

# Origin and evolution of the North Atlantic Oscillation

Received: 18 January 2024

Accepted: 21 February 2025

Published online: 03 March 2025

 Check for updates

Zhihong Song<sup>1</sup>, Ji Nie<sup>1,2,3</sup>✉, Panxi Dai<sup>4</sup>, Zhongxi Lin<sup>1</sup>, Jiaqi Guo<sup>1</sup>,  
Jiawenjing Lan<sup>1</sup>, Xiang Li<sup>1</sup>, Qifan Lin<sup>1</sup>, Zihan Yin<sup>1</sup>, Jun Yang<sup>1,2,3</sup>,  
Yonggang Liu<sup>1,2,3</sup>, Haijun Yang<sup>5</sup> & Yongyun Hu<sup>1,2,3</sup>✉

The North Atlantic Oscillation (NAO), the dominant mode of atmospheric variability in the North Atlantic region, plays a crucial role in weather and climate. Here, to investigate when the NAO emerged and how it evolved over geological timescales, we analyzed time-slice paleoclimate simulations during the breakup of the supercontinent Pangea, starting 160 million years ago (Ma). Our findings indicate that a present-day-like NAO mode gradually formed between 80 Ma and 60 Ma, driven by the expansion of the North Atlantic Ocean and the enhanced land-ocean contrast. This expansion led to a regime transition in Northern Hemisphere winter circulation, characterized by a westward shift of the North Atlantic jet, a strengthening of the North Atlantic high pressure and storm track, and the emergence of NAO-like variability. The confluence of orographic effects of the Rocky Mountains also contributed to the strengthening of the NAO. This study depicts the evolutionary history of the NAO over geological time and reveals its coherent relationship with the evolution of continents and orography.

The North Atlantic Oscillation (NAO), characterized by a dipole pressure anomaly over the North Atlantic<sup>1</sup>, is the dominant atmospheric variability mode in the Northern Hemisphere (NH) mid-high latitudes during winter time and has profound impacts on weather and climate. The phases of the NAO modulate the strength and position of the jet, resulting in significant weather anomalies over Europe and the Mediterranean<sup>2–4</sup>. The NAO also can impact remote regions such as East Asia<sup>5,6</sup>. Additionally, the NAO plays important roles in the climate system, affecting phenomena like the Atlantic Multidecadal Oscillation and Arctic sea ice<sup>7–13</sup>.

The NAO dominates atmospheric variability in the North Atlantic sector across various time scales<sup>1,14</sup>. The NAO index, based on instrumental station records, dates back to the 19th century<sup>15</sup> and can explain a significant portion of the variability in NH surface temperatures<sup>2</sup>. Over the past millennium, the phase shift of the NAO has been linked to the European climate transition from the Medieval Climate Anomaly to

the Little Ice Age<sup>16</sup>. Proxy reconstructions indicate the existence of the NAO since the early Holocene<sup>17,18</sup>. While the NAO is primarily controlled by atmospheric internal dynamics<sup>19</sup>, its spatial-temporal variation can be influenced by external forcings such as volcanic eruptions<sup>20</sup>, solar cycles<sup>21</sup>, and changes in surface boundary conditions<sup>22,23</sup>.

Previous studies have shown that surface boundary conditions, particularly the land-ocean contrasts and large-scale mountains, play a crucial role in shaping the NAO<sup>23–25</sup>. The land-ocean thermal contrasts and orographic features like the Rocky Mountains (RM) can force atmospheric stationary waves<sup>26,27</sup> and increase baroclinicity and eddy activity in the North Atlantic sector<sup>25,28,29</sup>. Idealized simulations suggest that both factors are pivotal in localizing storm tracks and the NAO<sup>23,30</sup>. Glaciers are also possible orographic factors; for example, continental ice sheets may have affected the NAO during the Last Glacial Maximum<sup>31</sup>.

Over geological time scales, continental distribution underwent drastic changes due to plate tectonics. When did the NAO first

<sup>1</sup>Laboratory for Climate and Ocean-Atmosphere Studies, Department of Atmospheric and Oceanic Sciences, School of Physics, Peking University, Beijing, China. <sup>2</sup>Institute of Ocean Research, Peking University, Beijing, China. <sup>3</sup>Institute of Carbon Neutrality, Peking University, Beijing, China. <sup>4</sup>Department of Atmospheric Sciences, School of Earth Sciences, Zhejiang University, Hangzhou, China. <sup>5</sup>Department of Atmospheric and Oceanic Sciences and Institute of Atmospheric Sciences, Fudan University, Shanghai, China. ✉e-mail: [jinnie@pku.edu.cn](mailto:jinnie@pku.edu.cn); [yyhu@pku.edu.cn](mailto:yyhu@pku.edu.cn)

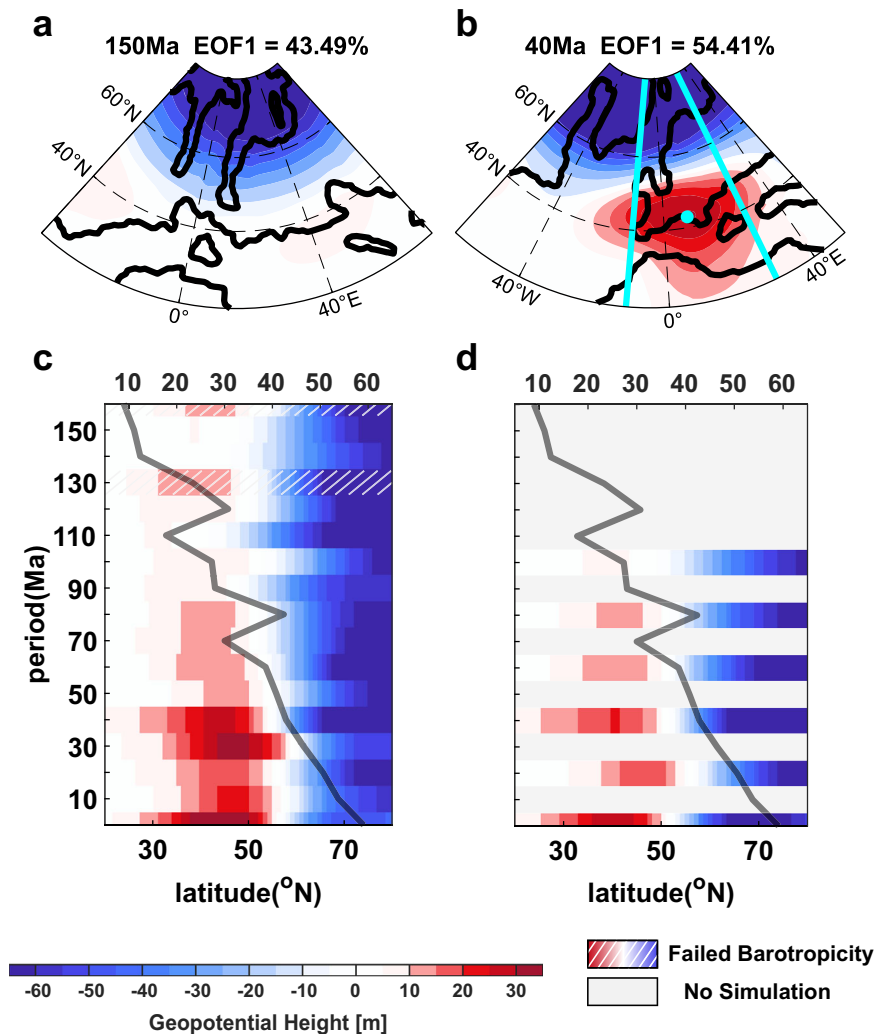


**Fig. 1 | The evolution of the leading empirical orthogonal function (EOF) pattern.** The leading EOF (EOF1) of wintertime geopotential height at the 1000 hPa level ( $Z_{1000}$ ) of (a) the 150 Ma and (b) the 40 Ma cases. The color indicates the zonally averaged EOF1 pattern for the paleoclimate simulations of (c) the default simulations and (d) the flatten-Rocky-Mountain simulations (NRM). The black solid

line is the average width (in units of longitude, corresponding to the upper x-axes) of the North Atlantic Ocean between 40°N and 60°N. In (c), the white diagonal denotes EOFs (160 Ma and 130 Ma) that failed to pass the criterion of barotropy. In (d), we simulated only the periods from the pre-industrial to 100 Ma at intervals of 20 Ma, and the periods not simulated are masked in grey.

emerge in geological timescales? How did the evolution of continental distribution alter the NAO in the past, and what is the key mechanism? These unexplored questions are the focus of this study. Here, with a set of time-slice paleoclimate simulations (Methods), we examine the origin and evolution of the NAO over geological timescales, specifically during the breakup of the supercontinent Pangea and the expansion of the North Atlantic Ocean since 160 million years ago (Ma). By answering the abovementioned questions, this study establishes a coherent relationship between continental configurations and the characteristics of the NAO over geological time.

## Results

### Origin and evolution of the NAO

We first obtain the leading empirical orthogonal function (EOF) of wintertime surface geopotential height anomalies over the North Atlantic sector in both the reanalysis data and paleoclimate simulations (Methods). The EOFs are normalized to ensure the standard deviation of the principal components is one. The leading EOF of the pre-industrial (PI) simulation exhibits a typical NAO pattern, closely matching the results from the reanalysis data (Fig. S1). This alignment,

consistent with previous studies<sup>32,33</sup>, validates the CESM's capability in simulating the NAO.

The leading EOFs in the paleoclimate simulations display notable variabilities. Fig. 1a, b shows two examples of the 150 Ma and 40 Ma, and Fig. S1 shows all the cases. As time period approaches PI, the spatial patterns of the EOFs increasingly resemble the meridional dipole of the modern NAO (Fig. S1). Before 80 Ma (except 130 Ma and 160 Ma), the midlatitude positive centers of the EOFs are too weak to be called NAO-like. An important feature of the modern NAO is its barotropic structure<sup>5</sup>. At 130 Ma and 160 Ma, the leading EOFs at the middle troposphere (Fig. S2) do not show meridional dipole patterns, thus, they failed to pass the criterion of barotropy. On the other hand, after 80 Ma, the leading EOFs exhibit similar meridional dipoles in the middle troposphere (Fig. S2). Given the lack of a strict threshold for paleoclimate NAO in the literature and the gradual change of the EOFs, we propose that a NAO-like mode emerges between 80 Ma and 60 Ma.

The evolution of the leading EOFs from a non-NAO-like pattern at 160 Ma to the modern NAO may be better demonstrated in a zonally averaged plot (Fig. 1c). Since all the EOFs have strong negative centers in high latitudes, the main difference among the EOFs is whether there is a localized and strong positive center in the midlatitudes (Fig. S1).

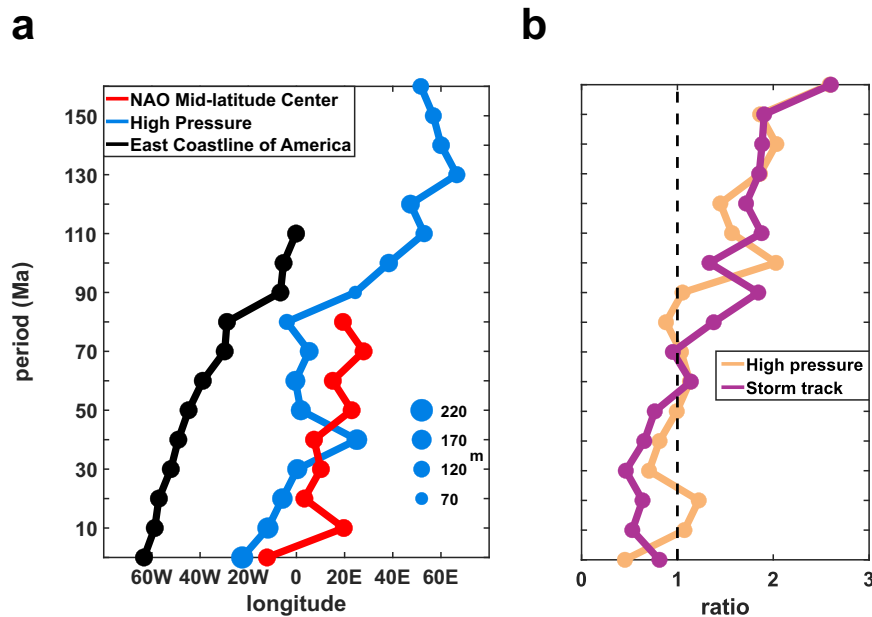


**Fig. 2 | The evolution of features of Northern Hemispheric winter circulation.** **a** the longitude of the midlatitude positive centers of the North Atlantic Oscillation (NAO)-like patterns (red dots), the centers of the 250 hPa North Atlantic high pressures (blue dots, with the size indicating the amplitude), and the mean longitudes of the east coastlines of the North America between 40°N and 60°N (black dots). **b** The area ratio of the North Pacific high pressure to the North Atlantic high

pressure and the North Pacific storm track to the North Atlantic storm track. In **(b)**, we first find the 80% percentile contour of the pressure anomalies from 20°N to the North Pole in each time period. Then, we calculate the ratio of the area enclosed by the 80% percentile contour over the North Pacific and North Atlantic region. The area ratio of the storm track is calculated in a similar way. Examples of the area calculations are in Fig. S6.

In Fig. 1c, for each paleoclimate EOF, we first identify the maximum of the midlatitude positive anomalies, then zonally average the EOF over a 20° band to the east and west (e.g., the cyan lines in Fig. 1b). Consistent with Fig. S1, Fig. 1c shows the gradual emergence of the NAO. In the following, we refer to an EOF with larger positive midlatitude anomalies as a stronger NAO to represent its resemblance to the modern NAO.

To obtain a causal explanation for the emergence and evolution of the NAO, we link them to the variations of external parameters of the climate system. The main differences in the external parameters across the simulated time periods are the CO<sub>2</sub> concentrations, continental distribution, and orography (i.e., large-scale mountains). The CO<sub>2</sub> concentrations largely determine the global mean temperature, while continental distribution and orography break the zonal symmetry of general circulation by introducing background stationary waves<sup>23,25,26,34</sup>. To examine the effects of climate, we conducted a set of simulations with fixed CO<sub>2</sub> at 10 times the PI level (FixCO<sub>2</sub>, Methods), which exhibit much weaker climate variation than the default simulations (Fig. S3a). The evolution of the leading EOFs over the North Atlantic in FixCO<sub>2</sub> shows a gradual emergence of an NAO-like pattern mode (Fig. S3b), similar to that in Fig. 1c. The cooling of the climate since 40 Ma seems to have greatly enhanced the NAO-like mode, consistent with results from current global warming studies<sup>35</sup>. It indicates that climate may modify the characteristics of the NAO<sup>35,36</sup>, but is unlikely to form the NAO itself. The impact of climate will be addressed in detail in a separate study. Here, we focus on the effects of continental distribution and orography on the evolution of the NAO under realistic paleoclimate history. In the following two sections, we demonstrate that the expansion of the North Atlantic Ocean was the main driver of the NAO's origination and that the presence of the RM likely enhanced the NAO substantially.

### Origination of the NAO by the expansion of the Atlantic Ocean

As an internal variability mode, the NAO is closely related to storm tracks, jet streams, and stationary waves<sup>23,24</sup>, whose regional features

are heavily influenced by continental configurations. Here, we show that the expansion of the North Atlantic Ocean leads to a regime transition in the NH winter circulation: the dominant region of transient eddy energy dissipation (represented by the storm track) shifts from the North Pacific to the North Atlantic, accompanied by the emergence of an NAO-like variability mode.

We first examine the NH winter stationary waves and their co-evolution with continental drift (Fig. S4). Throughout all periods, the NH exhibits a dominant wavenumber-2 pattern, corresponding to the two major continents. Beginning at 110 Ma, the North Atlantic Ocean expands. The west coast of Eurasia remains near 0°E, while the east coast of North America shifts westward. Prior to the expansion, the North Pacific high pressure is significantly stronger than the North Atlantic high pressure (Fig. S4a–e). As the North Atlantic Ocean expands, the land-ocean contrasts over the North Atlantic sector increase, and the North Atlantic high pressure strengthens and shifts westward (Figs. 2a, S4). At the same time, the North Pacific high pressure weakens relatively. The area ratio of the North Pacific high to the North Atlantic high (Fig. 2b, with examples of the calculation method in Fig. S6) clearly illustrates the shift of high-pressure centers from the Western Hemisphere to the Eastern Hemisphere with the expansion of the North Atlantic Ocean.

The jets and storm tracks undergo a similar transition (Fig. S5). Prior to the expansion of the North Atlantic Ocean (Fig. S5a–e), in line with the weak North Atlantic high pressure, the North Atlantic jet extends eastward to Eurasia, close to the entrance of the Eurasian jet. On the other hand, the strong North Pacific high leads to a wide jet gap over the North Pacific, where transient eddy energy dissipates and a strong North Pacific storm track forms. As time progresses, the westward expansion of the North Atlantic high pressure pushes the North Atlantic jet westward. Consequently, the jet gap over the North Atlantic widens, while it narrows over the North Pacific. This results in the weakening of the North Pacific storm track and strengthening of the North Atlantic storm track (Fig. 2b). A strong North Atlantic storm track corresponds to significant transient eddy energy

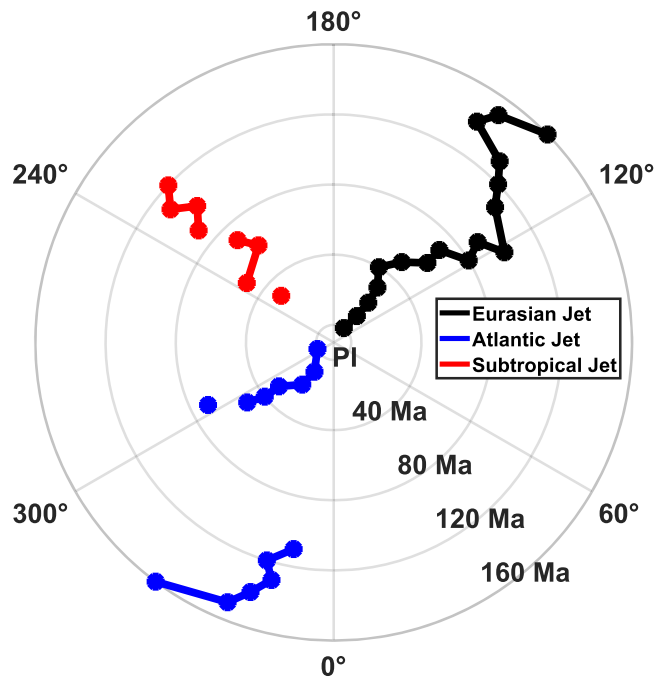


**Fig. 3 | The evolution of Northern Hemispheric winter jet cores.** The longitudes of 250 hPa jet cores (local maxima of zonal winds) of the Eurasian jet (black), North Atlantic jet (blue), and subtropical Pacific jet (red). From outer to inner, the circles denote time periods from 160 Ma to pre-industrial.

dissipation and increased jet meandering<sup>23,37,38</sup>, thus the emergence of the NAO.

The shift of the North Atlantic jet over time is shown in Fig. 3. It should be noted that the above discussion pertains to midlatitude jets. During 100 Ma to 60 Ma, a subtropical jet develops over the North Pacific and merges with the North Atlantic jet, eliminating a distinct North Atlantic jet core. However, since the subtropical jet is less associated with storm tracks, the argument regarding the westward shift of the North Atlantic jet remains unaffected.

A set of aquaplanet simulations with two rectangular lands (Methods) is conducted to test the proposed mechanism in an idealized world. In these simulations (Fig. S7), the distance between the two lands increases, analogous to the expansion of the North Atlantic Ocean. As examples, the leading EOF shows a NAO-like pattern for an ocean width of 60° (analogous to the PI), but not for 20° width (Fig. 4a, b). Figure 4c shows a summary of the idealized simulations. The NAO-like EOF emerges as the ocean between the two lands becomes wide enough (approximately greater than 40°), consistent with the results of paleoclimate simulations. The aquaplanet simulations shows a regime transition of circulation qualitatively similar with that in the paleoclimate simulation. As the two lands move away from each other, a warm and high-pressure anomaly emerges and gradually strengthens over the expanding ocean basin (Fig. S8). During the same time, a strong storm track develops (Fig. S9), and a NAO-like variability mode emerges (Fig. S7). The consistency between the idealized simulations and the paleoclimate simulations confirms that a sufficiently wide North Atlantic Ocean forms the NAO due to stationary waves induced by the thermal contrasts between the ocean and land.

### Strengthening of the NAO by the Rocky Mountains

Large orographic barriers, such as the Rocky Mountains, forms stationary waves by blocking the westerlies and inducing diabatic heating anomalies<sup>26,39,40</sup>. Modifying the orography of the RM in numerical simulations can substantially alter stationary wave, jet, and storm track<sup>25,41</sup>. The modern RM formed through complex geological

processes of mountain building and erosion<sup>42–44</sup>. Based on the paleogeography used in our simulations<sup>45</sup> (Fig. S10), the average height of the RM has gradually increased since 100 Ma (method, Fig. S10). To evaluate the effects of the RM on the NAO, we conducted sensitivity experiments with modified orography in both the idealized and realistic setups.

In the idealized simulations, we added a two-dimensional Gaussian-shaped mountain mimicking the RM, with average heights of 412 m, 620 m, 825 m, and 1237 m in the cases of TLO, TL20, and TL60, respectively. The leading EOFs of these simulations are shown in Fig. S11 and summarized in Fig. 4d. With a single continent (TLO), even the tallest mountain does not lead to an NAO-like mode. In TL20, a mountain with a height of 1237 m is able to form an NAO-like mode. In TL60, the NAO-like mode is strengthened when the mountain height exceeds 825 m. The mountain induces an orographic stationary wave that superimposes on the land-ocean-induced stationary wave (Fig. S12). The higher the mountain, the stronger the orographic wave. Another important factor is the phase match between the orographic and land-ocean-contrast stationary waves. In TLO, the two waves are nearly out of phase, while in TL20 and TL60, their phases largely match (Fig. S13). Despite differences in experimental design, our results agree with those of Gerber and Vallis (2009)<sup>23</sup>, highlighting the importance of the confluence of orographic and land-ocean-contrast waves in strengthening the NAO.

We also performed a set of high-resolution simulations in which the RM are flattened (NRM, method). Due to the limitation of computational resources, these simulations cover the period from the PI to 100 Ma with an interval of 20 Ma. The simulation results are shown in Fig. S14 and summarized in Fig. 1d. Comparing Fig. 1c and Fig. 1d, the removal of the RM leads to a notable weakening of the NAO-like mode from 40 Ma to PI. The effect of the RM is less significant from 60 Ma to 100 Ma, presumably because the NAO-like mode was weak and the RM were lower and narrower during these times. The orographic waves of RM are shown in Fig. S15. The results of the PI case are very similar to previous studies (e.g., Fig. 9 in Brayshaw et al. 2009<sup>25</sup>, Fig. 11 in Jiang and Yang 2011<sup>41</sup>). Throughout the examined time periods, the phases of the orographic waves approximately match those of the land-ocean-contrast stationary waves over the North Atlantic sector, indicating that the presence of the RM helps localize and strengthen the NAO. Compared with the idealized simulations, the results in the realistic setup are much noisier and more complex. Many factors may contribute to the complexity, such as the varying background flow and orographic features of the real RM. Still, the conclusions from the realistic and idealized sensitivity experiments agree that the RM may have strengthened the NAO since 40 Ma by inducing orographic waves that enhance the land-ocean-contrast wave.

## Discussion

This study simulates and examines the origin and evolution of the NAO on a geological timescale, spanning from the breakup of the supercontinent Pangea at 160 Ma to the present. By combining time-slice paleoclimate simulations and aquaplanet simulations, we demonstrate that the robust NAO-like variability mode emerges as the North Atlantic Ocean expands around 80 Ma to 60 Ma, associated with a regime transition of the NH winter circulation. The expansion of the North Atlantic Ocean enhances the land-ocean contrasts over the North Atlantic region. As a result, the North Atlantic high pressure strengthens, the North Atlantic jet moves westward, and the North Atlantic storm track enhances, leading to the emergence of the NAO-like mode. The presence of the Rocky Mountains also contributes to the strengthening of the NAO by inducing orographic stationary waves that superimposed on the land-ocean-contrast stationary waves. A schematic (Fig. 5) summarized the key circulation features associated with the NAO before and after the expansion of the North Atlantic Ocean.

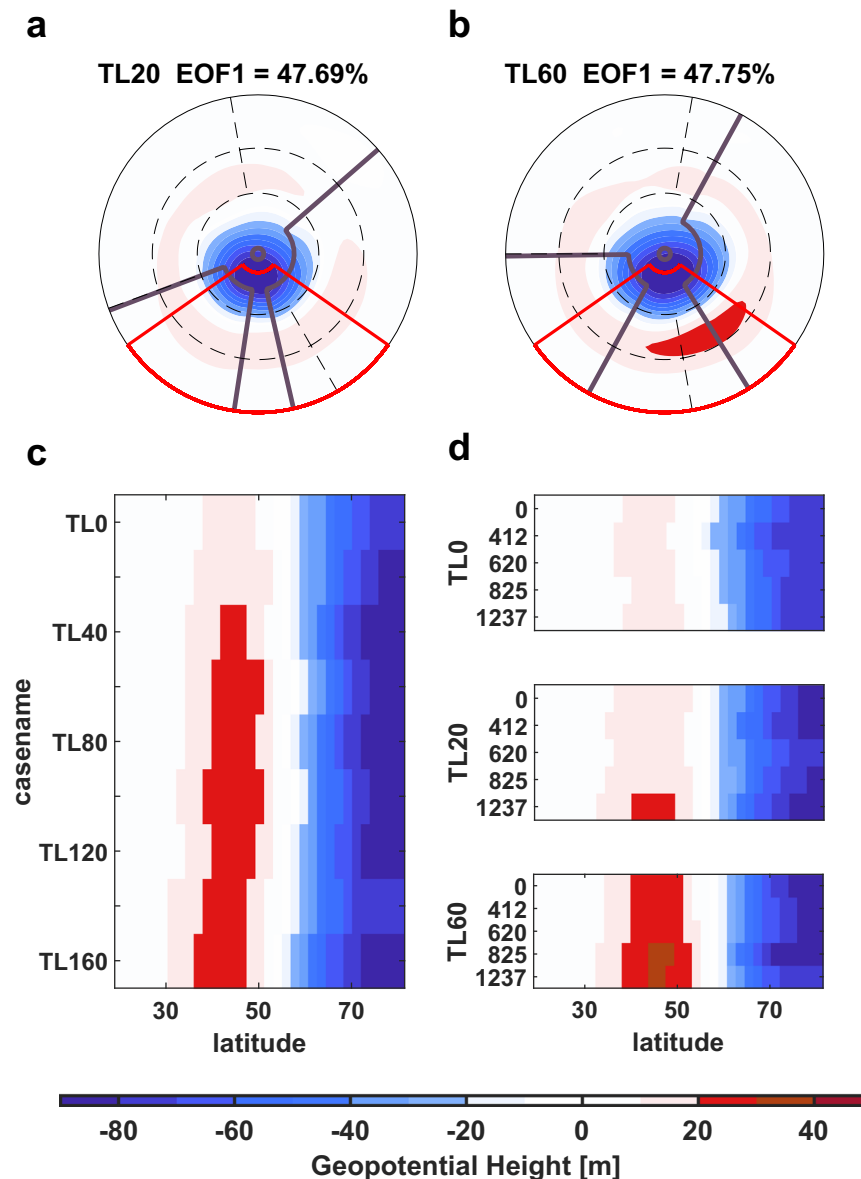


**Fig. 4 | The results of aquaplanet simulations.** The regression of wintertime  $Z_{1000}$  on the time series of the leading EOF of  $Z_{1000}$  over the red regional box for (a) the TL60 and (b) the TL20 cases. The black lines indicate the two rectangle continents. (c) The zonal averaged leading EOF pattern, similar with Fig. 1(c, d), for all the

aquaplanet simulations with flat surface. (d) The zonal averaged leading EOF pattern for the three sets of simulations with large-scale mountains. In (d), from top to the bottom are the results when the two continents are connected (TL0), 20° apart (TL20), and 60° apart (TL60), respectively.

This study systematically examined the co-evolution of the NH winter circulation with the continental configuration. The results have important implications on the fundamental question of how the geographic features of solid earth shape the regional atmospheric circulation and variability<sup>46</sup>. The regime transition of the NH winter circulation associated with the expansion of the North Atlantic Ocean may affect other atmospheric systems, such as the Pacific-North American teleconnection<sup>47</sup> and East Asia winter monsoon<sup>48</sup>. Here we only examined the monthly outputs, it is likely that our conclusions are also applicable to North Atlantic variability over other timescales, such as daily or interannual<sup>24,49</sup>, thus having implications on regional weather and climate.

Our results have some limitations that require further investigation. It would be interesting to explore the evolution of the leading EOF of extratropical geopotential variation across the entire NH extratropics, i.e., the Northern Annular Mode<sup>50</sup>. Some finer geographic features, such as ocean gateways that may affect ocean circulation and

sea surface temperature distribution, were not considered here. Our results show an enhancement of the NAO around 40 Ma, coinciding with the climate cooling and uplift of the RM. The uplift of the Tibetan Plateau also occurred around 40 Ma<sup>51</sup>, and studies have suggested nonlinear interactions between the orographic effects of the Tibetan Plateau and the RM<sup>26,41</sup>. The effects of the Tibetan Plateau and other nonlocal influences on the North Atlantic storm track<sup>52</sup> and the NAO are not explored in this study. Further investigations are needed to disentangle the roles of climate, the Tibetan Plateau, and the RM in shaping NH atmospheric circulation.

## Methods

### Reanalysis data and definition of the NAO

The reanalysis data from NCEP-2<sup>53</sup> are utilized. These data cover the period from 1979 to 2020 and are gridded at a  $2.5^\circ \times 2.5^\circ$  resolution with 17 vertical pressure levels. In this study, our focus is on the wintertime (December to February). The NAO is defined<sup>1,50,54</sup> by calculating

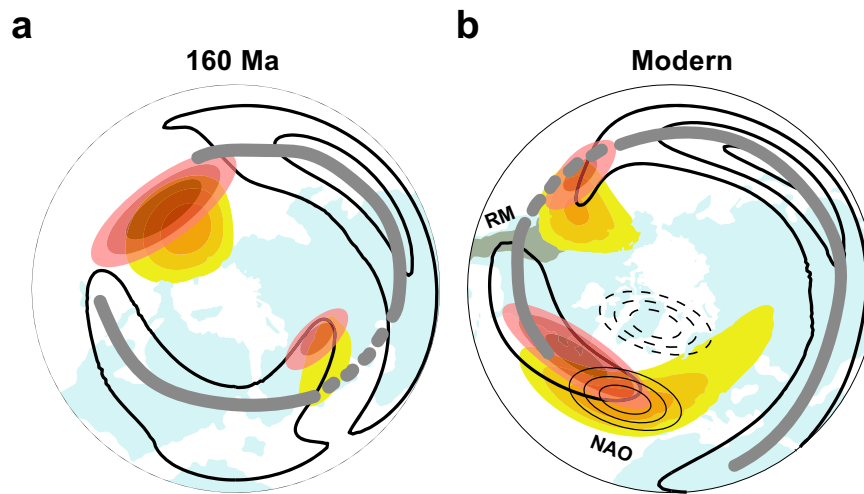


**Fig. 5 | A schematic of the circulation features.** **a** Is before and **(b)** is after the expansion of the North Atlantic Ocean. The thick black contour denotes upper tropospheric westerly jet, the yellow color denotes high-pressure anomalies, and the red color denotes storm track. The grey line denotes the waveguide of transient

eddy propagation. The continental distribution, westerly, and high-pressure anomalies in **(a)** are from the results of 160 Ma case, and in **(b)** are from the modern case. In **(b)**, the meridional dipole of NAO and the Rock Mountains (grey shading) are also plotted.

the leading mode of the EOF for the winter monthly  $Z_{1000}$  (geopotential height at the 1000 hPa level) over the North Atlantic region (20°N to 80°N, 70°W to 40°E for PI). For the paleoclimate period, we maintain the size of the regional box but shift its location so that it always centers on the North Atlantic Ocean. Our results are not sensitive to reasonable perturbations in the choices of the regional box. The modern NAO exhibits a robust equivalent barotropic structure<sup>1</sup>. With this in mind, we posed a barotropic requirement for the NAO, stating that both the leading EOFs of  $Z_{1000}$  and  $Z_{500}$  (geopotential height at the 500 hPa level) shall exhibit similar meridional dipole patterns. The EOFs at 160 Ma and 130 Ma do not pass this criterion and are not considered NAO-like modes (marked by the white diagonal in Fig. 1c).

### Paleoclimate simulations

Our main results are derived from a series of time-slice paleoclimate simulations using the Community Earth System Model 1.2.2<sup>55</sup> (CESM1.2.2). These time-slice simulations<sup>56</sup> cover the period from 160 Ma, predating the formation of the North Atlantic Ocean, to pre-industrial (PI), with a 10-million-year interval. The PI simulation's climatology reasonably aligns with observations<sup>56</sup>. Key differences between simulations lie in continental configurations and global mean temperature. Global mean surface temperatures for each era are tuned to match proxy reconstructions<sup>57</sup> by setting  $\text{CO}_2$  concentrations. Solar radiation increases linearly from 1344  $\text{W m}^{-2}$  at 160 Ma to 1361  $\text{W m}^{-2}$  at present. Paleogeographic maps are sourced from the paleo-digital elevation model<sup>45</sup>, which provides the continental distribution, bathymetric and topography maps on the simulated time periods. The evolution of the large topographic features, such as the Tibetan Plateau and the Rocky Mountains, and oceanic gateways, such as the Drake Passage and Tasmanian Passage, are included in the paleogeographic maps used in the paleoclimate simulations. The paleogeographic map is available at <https://zenodo.org/records/5460860>.

Each paleo period includes both low- and high-resolution simulations. The low-resolution simulations consist of atmosphere (CAM4, with a horizontal  $3.75^\circ \times 3.75^\circ$ ), ocean (POP2, with a horizontal resolution of g37), land (CLM4), sea-ice (CICE4) and river components (RTM), which are linked through a coupler. Since the paleogeographic maps of Scotese and Wright (2018) do not include information of ice sheets, there are no prescribed ice sheets in our simulation except the PI simulation that uses the CESM1.2.2's default ice sheets. The impact of

the lack of ice-sheets shall be small for this study, since the Greenland ice sheet emerges from 2.5 Ma<sup>58</sup>. The Antarctic ice-sheet emerges from 40 Ma<sup>59</sup>, however, it is too far away from the North Atlantic region. The low-resolution simulations are run to equilibrium (for several thousand model years) to obtain the climatological states. Then, the high-resolution simulations using an atmospheric model with a horizontal resolution of f09 ( $0.9375^\circ \times 1.25^\circ$ ) are driven by the prescribed climatological monthly mean sea surface temperatures (SSTs), sea-ice, and annual mean land vegetation, which are derived from the corresponding low-resolution simulations. Each high-resolution simulation also run to equilibrium, and we analyze the outputs of the last 60 years. The results of the low- and high-resolution simulations are similar. Here, we present the high-resolution simulations as the default simulations.

A set of simulations with fixed  $\text{CO}_2$  (short for FixCO2) is performed to examine the effect of background climate on the evolution of the NAO. These simulations follow the same setup as the default runs, except the  $\text{CO}_2$  concentration in all the time periods is fixed at 10 times the PI value. For each paleo time period, we also first run an atmosphere-ocean-coupled low-resolution simulation to obtain the climatological SSTs. Then, a high-resolution atmosphere model is driven by the climatology from the low-resolution simulations. The results of the FixCO2 high-resolution simulations are summarized in Fig. S3. Note that the global mean surface temperature in FixCO2 fluctuates with a standard deviation of 1.3 K, due to surface albedo changes associated with the evolution of continental configuration<sup>60</sup>.

A set of simulations with flattened Rocky Mountains (short for NRM) is performed to examine the effects of the RM on the evolution of the NAO. These simulations are the same with the default high-resolution simulations (driven by low-resolution simulations with various  $\text{CO}_2$ ), except we set the areas over the RM with a surface elevation above 300 meters to 300 meters. The other surface properties, such as vegetation, are unchanged. The NRM simulations are performed for the time period from PI to 100 Ma with an interval of 20 Ma. The results of the NRM simulations are summarized in Fig. 1d.

### Aquaplanet simulations

We conducted a series of aquaplanet simulations with CESM1.2.2 to explore the relationship between the width of the ocean basin and the NAO. Initially, we performed a slab ocean simulation (with a depth of 50 meters) with a prescribed ocean heat flux<sup>61</sup>. The seasonal cycle is

driven by an obliquity of 23.5°. Subsequently, a set of atmosphere-only simulations was run with SST prescribed as the monthly-mean SST obtained from the slab ocean simulation. Given the 50 m ocean depth, the seasonal cycle of SST in the slab ocean simulation lags behind observations by about 2 months<sup>61,62</sup>. This SST lag is adjusted in the fixed SST simulations. The fixed SST simulations also feature two rectangular continents covering 20°N–70°N with a width of 60° and 120°, respectively. These continents may analogously represent the North American and Eurasian continents. The land elevation is set at 50 m, and the surface vegetation is grassland. In each simulation, the distance between the two continents varies from 0° to 160° with intervals of 20°. These simulations are named Two-Lands-simulations (TL\*, where \* refers to the distance between the two lands). Each simulation runs for 210 years, with the monthly outputs of the last 150 years analyzed.

To examine the effect of the RM on the NAO, we performed additional experiments with RM-like mountains in the TLO, TL20, and TL60 cases. The mountains are two-dimensional gaussian shaped with a half width at half maximum of 5° in the zonal direction and 15° in the meridional direction. The latitude of the mountain peak is 45°N, and the longitude is 15° west to the coast line of the smaller continent. In TLO, we run four simulations with the mountain peak of 523 m, 786 m, 1050 m, and 1500 m. The corresponding average heights (following the calculation below) are 412 m, 620 m, 825 m, and 1237 m, respectively. The same is done for the TL20 and TL60 cases. Thus, there are 12 simulations in total with idealized mountains. The results of the NRM simulations are summarized in Fig. 4d.

### Calculation of the average height of the Rocky Mountains

Over geological time, the evolution of the orographic features of the RM is quite complicated (the gray dotted contours in Fig. S5). For simplicity, we calculate the average height of the RM as follows: first, we identify the peak of the RM between 30°N and 50°N. Next, we determine the highest grids at each latitude within a latitudinal band 5° north and south of the peak. Finally, we average the height across a meridional band 5° west and east of the peak at each latitude. The evolution of the average height of the RM is shown in Fig. S10. Different metrics of the RM height may yield different values, but the overall trends are similar.

### Data availability

The NCEP Reanalysis-2 data are available at (<https://psl.noaa.gov/data/gridded/data.ncep.reanalysis2.html>). The paleoclimate simulation data in this study are reported in and available at Li et al. (2022)<sup>56</sup>. The analyses data are available at <https://doi.org/10.5281/zenodo.14507022><sup>63</sup>.

### Code availability

The codes for the analyses are available at <https://doi.org/10.5281/zenodo.14507022><sup>63</sup>.

### References

- Hurrell, J. W., Kushnir, Y., Ottersen, G. & Visbeck, M. An overview of the North Atlantic oscillation. *Geophys. Monogr. Ser.* **134**, 1–36 (2003).
- Hurrell, J. W. & Van Loon, H. Decadal variations in climate associated with the North Atlantic Oscillation. *Clim. Change* **36**, 301–326 (1997).
- Thompson, D. W. & Wallace, J. M. Regional climate impacts of the Northern Hemisphere annular mode. *Science* **293**, 85–89 (2001).
- Casado, M. et al. Impact of precipitation intermittency on NAO-temperature signals in proxy records. *Clim* **9**, 871–886 (2013).
- Watanabe, M. Asian jet waveguide and a downstream extension of the North Atlantic Oscillation. *J. Clim.* **17**, 4674–4691 (2004).
- Li, J. et al. Influence of the NAO on wintertime surface air temperature over East Asia: Multidecadal variability and decadal prediction. *Adv. Atmos. Sci.* **39**, 625–642 (2022).
- Visbeck, M. H., Hurrell, J. W., Polvani, L. & Cullen, H. M. The North Atlantic Oscillation: past, present, and future. *PNAS* **98**, 12876–12877 (2001).
- Li, J., Sun, C. & Jin, F. F. NAO implicated as a predictor of Northern Hemisphere mean temperature multidecadal variability. *Geophys. Res. Lett.* **40**, 5497–5502 (2013).
- Peings, Y. & Magnusdottir, G. Forcing of the wintertime atmospheric circulation by the multidecadal fluctuations of the North Atlantic Ocean. *Environ. Res. Lett.* **9**, 034018 (2014).
- Sun, C., Li, J. & Jin, F.-F. A delayed oscillator model for the quasi-periodic multidecadal variability of the NAO. *Clim. Dyn.* **45**, 2083–2099 (2015).
- Delworth, T. L. & Zeng, F. The impact of the North Atlantic Oscillation on climate through its influence on the Atlantic meridional overturning circulation. *J. Clim.* **29**, 941–962 (2016).
- Delworth, T. L. et al. The North Atlantic Oscillation as a driver of rapid climate change in the Northern Hemisphere. *Nat. Geosci.* **9**, 509–512 (2016).
- Wills, R. C., Armour, K. C., Battisti, D. S. & Hartmann, D. L. Ocean-atmosphere dynamical coupling fundamental to the Atlantic multidecadal oscillation. *J. Clim.* **32**, 251–272 (2019).
- Feldstein, S. B. The timescale, power spectra, and climate noise properties of teleconnection patterns. *J. Clim.* **13**, 4430–4440 (2000).
- Jones, P. D., Jonsson, T. & Wheeler, D. Extension to the North Atlantic Oscillation using early instrumental pressure observations from Gibraltar and south-west Iceland. *Int. J. Climatol.* **17**, 1433–1450 (1997).
- Trouet, V. et al. Persistent positive North Atlantic oscillation mode dominated the Medieval Climate Anomaly. *Science* **324**, 78–80 (2009).
- Olsen, J., Anderson, N. J. & Knudsen, M. F. Variability of the North Atlantic Oscillation over the past 5,200 years. *Nat. Geosci.* **5**, 808–812 (2012).
- Becker, L. W. et al. Palaeo-productivity record from Norwegian Sea enables North Atlantic Oscillation (NAO) reconstruction for the last 8000 years. *npj Clim. Atmos. Sci.* **3**, 42 (2020).
- Vallis, G. K., Gerber, E. P., Kushner, P. J. & Cash, B. A. A mechanism and simple dynamical model of the North Atlantic Oscillation and annular modes. *J. Atmos. Sci.* **61**, 264–280 (2004).
- Christiansen, B. Volcanic eruptions, large-scale modes in the Northern Hemisphere, and the El Niño–Southern Oscillation. *J. Clim.* **21**, 910–922 (2008).
- Kuroda, Y., Kodera, K., Yoshida, K., Yukimoto, S. & Gray, L. Influence of the solar cycle on the North Atlantic Oscillation. *J. Geophys. Res.: Atmos.* **127**, e2021JD035519 (2022).
- Rodwell, M. J., Rowell, D. P. & Folland, C. K. Oceanic forcing of the wintertime North Atlantic Oscillation and European climate. *Nature* **398**, 320–323 (1999).
- Gerber, E. P. & Vallis, G. K. On the zonal structure of the North Atlantic Oscillation and annular modes. *J. Atmos. Sci.* **66**, 332–352 (2009).
- Vallis, G. K. & Gerber, E. P. Local and hemispheric dynamics of the North Atlantic Oscillation, annular patterns and the zonal index. *Dyn. Atmos. Oceans* **44**, 184–212 (2008).
- Brayshaw, D. J., Hoskins, B. & Blackburn, M. The basic ingredients of the North Atlantic storm track. Part I: Land–sea contrast and orography. *J. Atmos. Sci.* **66**, 2539–2558 (2009).
- Held, I. M., Ting, M. & Wang, H. Northern winter stationary waves: Theory and modeling. *J. Clim.* **15**, 2125–2144 (2002).
- Chang, E. K. Diabatic and orographic forcing of northern winter stationary waves and storm tracks. *J. Clim.* **22**, 670–688 (2009).
- Cash, B. A., Kushner, P. J. & Vallis, G. K. Zonal asymmetries, teleconnections, and annular patterns in a GCM. *J. Atmos. Sci.* **62**, 207–219 (2005).

29. Brayshaw, D. J., Hoskins, B. & Blackburn, M. The basic ingredients of the North Atlantic storm track. Part II: Sea surface temperatures. *J. Atmos. Sci.* **68**, 1784–1805 (2011).
30. Son, S.-W., Ting, M. & Polvani, L. M. The effect of topography on storm-track intensity in a relatively simple general circulation model. *J. Atmos. Sci.* **66**, 393–411 (2009).
31. Justino, F. & Peltier, W. R. The glacial North Atlantic Oscillation. *Geophys. Res. Lett.* **32**, eadh1106 (2005).
32. Wang, Z., Li, Y., Liu, B. & Liu, J. Global climate internal variability in a 2000-year control simulation with Community Earth System Model (CESM). *Chin. Geogr. Sci.* **25**, 263–273 (2015).
33. Deser, C., Hurrell, J. W. & Phillips, A. S. The role of the North Atlantic Oscillation in European climate projections. *Clim. Dyn.* **49**, 3141–3157 (2017).
34. Shaw, T. A., Miyawaki, O. & Donohoe, A. Stormier Southern Hemisphere induced by topography and ocean circulation. *PNAS* **119**, e2123512119 (2022).
35. Hamouda, M. E., Pasquero, C. & Tziperman, E. Decoupling of the Arctic Oscillation and North Atlantic Oscillation in a warmer climate. *Nat. Clim. Change* **11**, 137–142 (2021).
36. Rind, D., Perlwitz, J., Lonergan, P. & Lerner, J. AO/NAO response to climate change: 2. Relative importance of low-and high-latitude temperature changes. *J. Geophys. Res.: Atmos.* **110**, D12108 (2005).
37. Rogers, J. C. North Atlantic storm track variability and its association to the North Atlantic Oscillation and climate variability of northern Europe. *J. Clim.* **10**, 1635–1647 (1997).
38. Hakim, G. J. Developing wave packets in the North Pacific storm track. *Mon. Weather Rev.* **131**, 2824–2837 (2003).
39. Manabe, S. & Terpstra, T. B. The effects of mountains on the general circulation of the atmosphere as identified by numerical experiments. *J. Atmos. Sci.* **31**, 3–42 (1974).
40. Valdes, P. J. & Hoskins, B. J. Nonlinear orographically forced planetary waves. *J. Atmos. Sci.* **48**, 2089–2106 (1991).
41. Jiang, R. & Yang, H. Roles of the Rocky Mountains in the Atlantic and Pacific Meridional Overturning Circulations. *J. Clim.* **34**, 6691–6703 (2021).
42. Ruddiman, W., Prell, W. & Raymo, M. Late Cenozoic uplift in southern Asia and the American West: Rationale for general circulation modeling experiments. *J. Geophys. Res.: Atmos.* **94**, 18379–18391 (1989).
43. Erslev, E. A., Schmidt, C. & Chase, R. Thrusts, back-thrusts and detachment of Rocky Mountain foreland arches. *Spec. Pap. Geol. Soc. Am.* **280**, 339–358 (1993).
44. Herold, N. et al. A suite of early Eocene (~55 Ma) climate model boundary conditions. *Geosci. Model Dev.* **7**, 2077–2090 (2014).
45. Scotese, C. R. & Wright, N. PALEOMAP paleodigital elevation models (PaleoDEMs) for the Phanerozoic. *Paleomap Proj*, [www.earthbyte.org/paleodem-resource-scotese-and-wright-2018/](http://www.earthbyte.org/paleodem-resource-scotese-and-wright-2018/) (2018).
46. Han, J. et al. Continental drift shifts tropical rainfall by altering radiation and ocean heat transport. *Sci. Adv.* **9**, eadf7209 (2023).
47. Honda, M. & Nakamura, H. Interannual seesaw between the Aleutian and Icelandic lows. Part II: Its significance in the interannual variability over the wintertime Northern Hemisphere. *J. Clim.* **14**, 4512–4529 (2001).
48. Chan, J. C. & Li, C. in *East Asian Monsoon* 54–106 (World Scientific, 2004).
49. Cash, B. A., Kushner, P. J. & Vallis, G. K. The structure and composition of the annular modes in an aquaplanet general circulation model. *J. Atmos. Sci.* **59**, 3399–3414 (2002).
50. Thompson, D. W. & Wallace, J. M. The Arctic Oscillation signature in the wintertime geopotential height and temperature fields. *Geophys. Res. Lett.* **25**, 1297–1300 (1998).
51. Rowley, D. B. & Currie, B. S. Palaeo-altimetry of the late Eocene to Miocene Lunpola basin, central Tibet. *Nature* **439**, 677–681 (2006).
52. Swanson, K. L. Storm track dynamics. *Glob. Circ. Atmos.* **78**, 103 (2007).
53. Kanamitsu, M. et al. Ncep–doe amip-ii reanalysis (r-2). *Bull. Am. Meteorol. Soc.* **83**, 1631–1644 (2002).
54. Thompson, D. W., Lee, S. & Baldwin, M. P. Atmospheric processes governing the northern hemisphere annular mode/North Atlantic oscillation. *North Atl. Oscillation: Clim. Significance Environ. impact* **134**, 81–112 (2003).
55. Hurrell, J. W. et al. The community earth system model: a framework for collaborative research. *Bull. Am. Meteorol. Soc.* **94**, 1339–1360 (2013).
56. Li, X. et al. A high-resolution climate simulation dataset for the past 540 million years. *Sci. Data* **9**, 371 (2022).
57. Scotese, C. Phanerozoic Temperature Curve. *PALEOMAP Project* (2015).
58. Alley, R. B. et al. History of the Greenland Ice Sheet: paleoclimatic insights. *Quat. Sci. Rev.* **29**, 1728–1756 (2010).
59. Zachos, J., Pagani, M., Sloan, L., Thomas, E. & Billups, K. Trends, rhythms, and aberrations in global climate 65 Ma to present. *Science* **292**, 686–693 (2001).
60. Li, X. et al. Climate variations in the past 250 million years and contributing factors. *Paleoceanogr. Paleoclimatol.* **38**, e2022PA004503 (2023).
61. Yin, Z. & Nie, J. Monsoon seasonality advanced by opposite-hemisphere continental drift. *Geophys. Res. Lett.* **49**, e2022GL100114 (2022).
62. Donohoe, A., Frierson, D. M. & Battisti, D. S. The effect of ocean mixed layer depth on climate in slab ocean aquaplanet experiments. *Clim. Dyn.* **43**, 1041–1055 (2014).
63. Song, Z. et al. Origin and Evolution of the North Atlantic Oscillation [Data set]. Zenodo. <https://doi.org/10.5281/zenodo.14507022> (2024).

## Acknowledgements

This research was supported by the National Natural Science Foundation of China (42488201 to Y.H. and J.N., and 42375057 to J.N.) and the Beijing Natural Science Foundation (JQ23037 to J.N.). This is a contribution to the Deep-time Digital Earth.

## Author contributions

J.N., Y.H., and Z.S. designed and performed the study. Z.S., J.G., J.L., X.L., Q.L., and Z.Y. carried out simulations. Z.S. analyzed the data. J.N., Y.H., Z.S. interpreted the results, and P.D., Z.L., J.Y., Y.L., and H.Y. provided inputs. J.N. wrote the paper with contributions from all authors.

## Competing interests

The authors declare no competing interests.

## Additional information

**Supplementary information** The online version contains supplementary material available at <https://doi.org/10.1038/s41467-025-57395-4>.

**Correspondence** and requests for materials should be addressed to Ji Nie or Yongyun Hu.

**Peer review information** *Nature Communications* thanks the anonymous reviewers for their contribution to the peer review of this work. A peer review file is available.

**Reprints and permissions information** is available at <http://www.nature.com/reprints>

**Publisher's note** Springer Nature remains neutral with regard to jurisdictional claims in published maps and institutional affiliations.

**Open Access** This article is licensed under a Creative Commons Attribution-NonCommercial-NoDerivatives 4.0 International License, which permits any non-commercial use, sharing, distribution and reproduction in any medium or format, as long as you give appropriate credit to the original author(s) and the source, provide a link to the Creative Commons licence, and indicate if you modified the licensed material. You do not have permission under this licence to share adapted material derived from this article or parts of it. The images or other third party material in this article are included in the article's Creative Commons licence, unless indicated otherwise in a credit line to the material. If material is not included in the article's Creative Commons licence and your intended use is not permitted by statutory regulation or exceeds the permitted use, you will need to obtain permission directly from the copyright holder. To view a copy of this licence, visit <http://creativecommons.org/licenses/by-nc-nd/4.0/>.

© The Author(s) 2025